Voltage losses in zero-gap alkaline water electrolysis

Haverkort, J. W.; Rajaei, H.

DOI
10.1016/j.jpowsour.2021.229864

Publication date
2021

Document Version
Final published version

Published in
Journal of Power Sources

Journal of Power Sources 497 (2021) 229864

Contents lists available at ScienceDirect

Journal of Power Sources

journal homepage: www.elsevier.com/locate/jpowsour

Voltage losses in zero-gap alkaline water electrolysis

J.W. Haverkort *, H. Rajaei

Process & Energy Department, Delft University of Technology, Leeghwaterstraat 39, 2628 CB Delft, The Netherlands

HIGHLIGHTS

- Bubble and concentration overpotential quantification for a zero-gap electrolyzer.
- An inactive electrode front explains the anomalously large separator resistance.
- An additional ohmic drop arises transiently, likely due to gas bubbles.
- Introducing a 0.2 mm gap strongly reduces the resistance.
- Local hydroxide depletion gives large losses at low electrolyte concentrations.

GRAPHICAL ABSTRACT

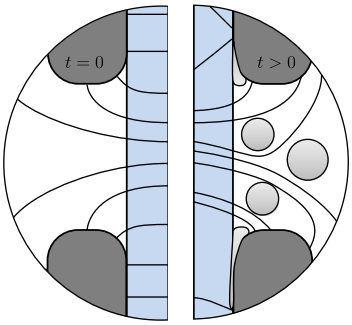

ARTICLE INFO

Keywords:
Alkaline water electrolysis
Zero-gap
Bubble Overpotential
Concentration overpotential
Zirfon PERL

ABSTRACT

Reducing the gap between the electrodes and diaphragm to zero is an often adopted strategy to reduce the ohmic drop in alkaline water electrolyzers for hydrogen production. We provide a thorough account of the current–voltage relationship in such a zero-gap configuration over a wide range of electrolyte concentrations and current densities. Included are voltage components that are not often experimentally quantified like those due to bubbles, hydroxide depletion, and dissolved hydrogen and oxygen. As is commonly found for zero-gap configurations, the ohmic resistance was substantially larger than that of the separator. We find that this is because the relatively flat electrode area facing the diaphragm was not active, likely due to separator pore blockage by gas, the electrode itself, and or solid deposits. Over an e-folding time-scale of ten seconds, an additional ohmic drop was found to arise, likely due to gas bubbles in the electrode holes. For electrolyte concentrations below 0.5 M, an overpotential was observed, associated with local depletion of hydroxide at the anode. Finally, a high supersaturation of hydrogen and oxygen was found to significantly increase the equilibrium potential at elevated current densities. Most of these voltage losses are shown to be easily avoidable by introducing a small 0.2 mm gap, greatly improving the performance compared to zero-gap.

1. Introduction

Modern alkaline water electrolyzers for hydrogen production are designed for ever higher current densities. The cost of electrodes, diaphragms or membranes, and bipolar plates scale with the geometrical electrode area, while the amount of hydrogen that is produced is proportional to the current. This makes operating at high current densities attractive. However, high current densities also make ohmic losses relatively more important.

A way to reduce ohmic losses is to position the electrodes directly adjacent to the separator in a so-called zero-gap configuration, inspired by fuel cell technology [1], see Fig. 1. It was first applied in a commercial electrolyzer by Zdansky–Lonza in the 1950s in a design that was later taken over by Lurgi [2]. Since then, most manufacturers

* Corresponding author.
E-mail address: J.W.Haverkort@tudelft.nl (J.W. Haverkort).
URL: https://jwhaverkort.weblog.tudelft.nl/ (J.W. Haverkort).

https://doi.org/10.1016/j.jpowsour.2021.229864
Received 29 January 2021; Received in revised form 26 March 2021; Accepted 29 March 2021
Available online 9 April 2021

Nomenclature

AR	Areal electronic resistance [Ωm^2]
b_i	Tafel slope $RT/\alpha_i F$ [V]
c	Electrolyte concentration [M]
E	Voltage [V]
E_0	Onset potential in Eq. (7) [V]
j	Current density [A/m^2]
j_*	Superficial exchange current density [A/m^2]
j_{eq}	Characteristic current density in Eq. (7) [A/m^2]
l	Effective ohmic thickness in Eq. (4) [m]
l_s	Separator thickness $\approx (5 \pm 0.5) \cdot 10^{-4}$ [m]
T	Temperature ≈ 300 [K]
t	Time [s]

Constants

F	Faraday constant 96485.3329 [C/mol]
R	Gas constant 8.31446 [J/mol/K]

Greek variables

α	Charge transfer coefficient [–]
ϵ	Separator porosity $\approx 0.5 \pm 0.1$ [–]
ϵ_e	Electrode open-hole fraction $\approx 1/3$ [–]
η	Activation overpotential [V]
κ	Electrolyte conductivity [S/m]
τ	Separator tortuosity [–]

Subscripts

a	Anode
b	Bubbles
c	Cathode
e	Electrodes
i	Index $i = a$ or c for anode or cathode
t	Transient
eq	Equilibrium
lim	Limiting, see Eq. (9)

have adopted this strategy [3]. It is generally assumed that a zero gap minimizes the ohmic losses [4]. However, the ohmic resistance in zero-gap configurations was consistently found to be much higher than that of the separator, awaiting a generally accepted explanation [5].

There has been some discussion in the literature about where gases evolve in a zero-gap configuration. Ref. [6] uses partially PTFE-covered electrodes to conclude that the majority of the gas evolution occurs at the electrode area facing the separator. Possibly, gas bubbles could escape here by capillary action through the fibers of the felt separator and or a small unintentional gap. In contrast, Ref. [7] states that the electrode area facing the diaphragm will be largely inactive due to coverage by a gas film. A schematic illustration of the resulting current lines is provided in, for example, Refs. [6,8] and Fig. 1. Ref. [9] stresses the importance of a good wettability of the diaphragm to avoid this so-called gas blanketing effect.

To avoid corrosion deposits *and* blanketing, Ref. [10] introduces filaments that are aligned with the upwards bubble movement and have a preferred thickness of around 0.2 mm. Refs. [6,11] mention that electrode openings of similar magnitude are required to avoid trapping of hydrogen bubbles, and larger ones for oxygen bubbles. In Ref. [12] a gap of at least this magnitude is used in testing various diaphragms and membranes.

Besides increasing the ohmic losses, trapped gas can also cause corrosion deposits [13], increased separator deterioration through hot-spots [14], and voltage fluctuations [15]. The zero-gap configuration has been associated with increased separator damage and gas cross-over [16].

Developed in the 1990s to replace asbestos diaphragms, a popular commercially available separator is Zirfon PERL produced by Agfa [17–21]. Owing to its polysulfone backbone, it is strong, and it has a relatively low-cost [22]. The hydrophilic ZrO_2 in Zirfon PERL improves the wettability [14,17,23,24]. However, Ref. [23] finds a rather low pore interconnectivity, bubble-point pressure, and wettability. This may cause incomplete wetting and perhaps even allow gas to enter the separator and increase the resistance [5,25,26]. Relatively high overpotentials, using Zirfon PERL in a zero-gap configuration, were attributed to gas blanketing [26]. Similarly, use of the hydrophilic separator material Celgard 2500 in a zero-gap configuration gave rise to an anomalously high resistive overpotential of about 100 mV at 10^3 A/m^2, attributed to "*the ohmic resistance of the "zero-gap", to imperfect wetting of the active layers, and to larger gas bubbles effects*" [25]. Application of a modest overpressure of the order of 1 bar was found to strongly decrease these losses. [25,27]

Various papers consider the effect of gas bubbles in the traditional electrolyzer configuration with an electrode-separator gap; including various reviews [28–31], experimental studies [32,33], and theoretical analyses [33–35], mostly focusing on the additional ohmic drop introduced by bubbles [14,34,36,37]. The additional overpotential due to bubbles reducing the reaction area was found to be relatively small, less than 5 mV at 10^3 A/m^2 [38] on a small vertical cylindrical electrode in an acidic electrolyte.

In the present work we add to the very little quantitative results that can be found on the effect of gas bubbles in zero-gap systems. We find that gas formation leads to a sizeable additional ohmic drop that builds up transiently over the order of ten seconds. An often overlooked voltage loss that we also consider is the increase in equilibrium potential due to dissolved hydrogen and oxygen. Under alkaline conditions the following redox reactions take place

$$4H_2O + 4e^- \rightarrow 4OH^- + 2H_2, \quad \text{(cathode)} \tag{1}$$

$$4OH^- \rightarrow 2H_2O + O_2 + 4e^- \quad \text{(anode)}. \tag{2}$$

Although the product gases have a very low saturation concentration, especially at high electrolyte concentrations, they can be present at very large supersaturations. Refs. [39,40] find hydrogen concentrations up to 120 mM, well over a hundred times the solubility. The associated potential increases approximately logarithmically with increasing current density. This is explained by dissolved hydrogen that is removed from the surface by mass transfer, giving a so-called 'gas evolution efficiency' smaller than one [41,42]. For current densities above 10^3 A/m^2, potential increases up to 70 mV have been measured [39,40].

There are several ways by which the transport of dissolved and gaseous products away from the electrodes can be increased, most obviously and effectively using flow. This may be flow-through the electrode, normal to the current [43], parallel to the current [44] or flow-by, where slug flow was found to increase mass transfer [45]. Promising alternatives include superaerophobic or superhydrophilic electrodes [46], partially 'liquid-free' or 'single irriguous' operation [17,47] or 'bubble-free' operation using hydrophobic diffusion layers [25,48–50]. Somewhat more experimental ideas include the use of pressure swings [51], ultrasound [52], or magnetic fields [53].

A final, rarely considered, loss that we include is that due to hydroxide depletion, which is a reactant in Eq. (2) at the anode. Recent studies showed that, using a separated anolyte and catholyte, *global* depletion of hydroxide of the anolyte can occur, leading to a limiting current density [54,55]. Here we show that at low electrolyte concentrations there can also be *local* depletion, giving rise to very large concentration overpotentials.

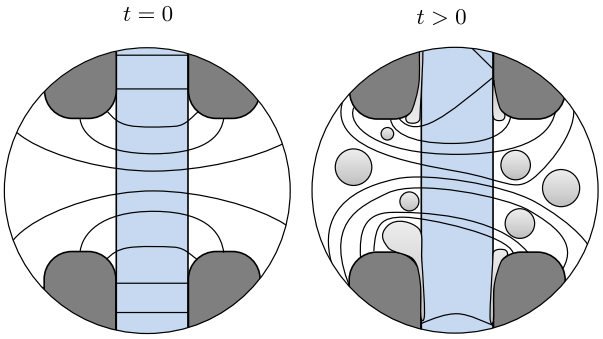

Fig. 1. An idealized schematic of possible low current density streamlines through the separator (light blue) between two electrodes (dark gray) at $t = 0$ immediately after the current is switched on and no bubbles (light gray) have yet formed (left) compared to some time later where the current lines have to go around the generated bubbles (right). Disclaimers: anode and cathode holes will not generally be this aligned; at higher current densities and in 3D the streamlines can stay closer to the separator; gas formation between the separator and diaphragm is speculative.

Simple semi-empirical fitting models are often used to predict the behavior of laboratory cells [37,56] as well as advanced water electrolyzers [57,58], so-called for their zero-gap, active electrodes, elevated temperatures and often elevated pressures. Here we extend such empirical relations to hold over a wide range of electrolyte concentrations and current densities by including the effect of bubbles, dissolved gas products, and concentration polarization due to hydroxide depletion.

2. Materials and methods

Fig. 2 shows the used cell configuration. A sub-microporous polysulfone-supported ZrO_2-based separator (Zirfon PERL, Agfa-Gevaert NV) with a thickness of 500 ± 50 μm was used, with a porosity of 0.5±0.1 [59]. This diaphragm was sandwiched between two equal 0.5 mm thick expanded metal electrodes of 10 cm^2 (Permascand AB) with main active components Ruthenium and Nickel oxides [27,60,61] and containing eye-shaped holes of approximately 3 × 1 mm. These layers were bolted together between two 6 mm thick PMMA plates. The assembly was immersed in a beaker of 13 cm diameter, filled with electrolyte to a height of about 8 cm to cover the electrode and separator area.

We used conductivities $\kappa_n = 1.445\left(\sqrt{2}\right)^n$ S/m from $\kappa_1 = 2.04$ S/m to $\kappa_{11} = 65.4$ S/m, by varying the potassium hydroxide (KOH) concentration from $c = 0.08$ M to 6 M using the formula [62]

$$\kappa = -204c - 0.28c^2 + 0.5332cT + 20720\frac{c}{T} + 0.1043c^3 - 3\cdot 10^{-5}c^2T^2, \quad (3)$$

with κ in S/m, c in M, inserting $T = 300$ K. We note that the original Ref. [63] has $-204.1c$ as the first term.

The anodic and cathodic Tafel slopes and exchange current densities were determined from an experiment using a 6 M electrolyte concentration, measuring the potential difference between the electrodes and that of a copper wire, inserted into the adjacent electrolyte as shown in Fig. 2. More details can be found in the supplementary data of Appendix A.

A constant current was applied using a BK Precision 9151 with an accuracy of 0.1%+ 15 mA. The used current densities were distributed from $j \approx 10$ A/m^2 up to $j = 10^4$ A/m^2, multiplying with $\sqrt{2}$ for every subsequent value. Using the same geometric progression as the conductivity allowed us to compare equal j/κ at different electrolyte concentrations, without interpolation. Each current density was maintained for 120 s, followed by 300 s of zero current, after which a higher current was applied. The same series was repeated in descending order of current density. No significant differences between the ascending and descending runs were found in the cell voltage. The cell voltage was recorded every second using a Madgetech RFVolt2000 A digital voltmeter with an accuracy of 0.05%, using separate clamps directly attached the electrodes. Although the cell voltage became stable well within a minute, for the below plots we used the value after 100 s, using the average of the values obtained during the ascending and descending runs. To further test the reproducibility we performed an additional run at a different occasion and location, in descending current density order, using a battery cycling system (Biologic, BCS-815, < 0.7% accuracy in current).

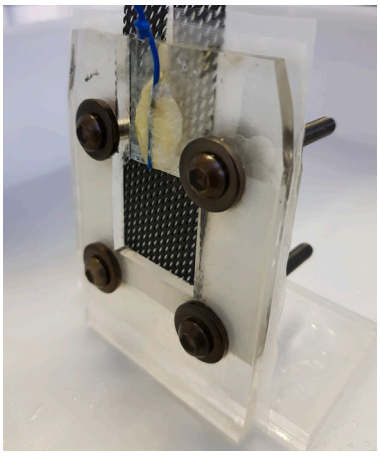

Fig. 2. The cell configuration showing the white separator, black electrodes, and transparent PMMA layers. Shown is the 'almost-zero-gap' configuration with two 0.2 mm thick nylon spacers visible between the electrodes and the separator. Squares, the size of the electrodes, have been cut out of the spacers. The blue copper wire, together with a similar one at the other side, was used as a pseudo-reference electrode, and to measure the electrolyte potential drop over the separator. The power supply and voltmeters are connected with separate crocodile clamps to the parts of the electrodes sticking out from the top.

3. Model

We introduce the following semi-empirical expression to model the cell voltage

$$E_{\text{cell}} = E_{\text{eq}} + \frac{jl}{\kappa} + ARj + \eta. \quad (4)$$

Here E_{eq} is the equilibrium cell voltage obtained immediately after switching off the current density j. The electrolyte losses are described by Ohm's law using an effective length-scale l. Additional linear losses that do not scale inversely proportional to the electrolyte conductivity κ are included using an areal resistance AR. Finally, the activation overpotential $\eta = \eta_c + \eta_a + \eta_{\text{lim}}$ where, with $i = c$ and a,

$$\eta_i = b_i \operatorname{asinh}\left(\frac{j}{2j_{*i}}\right). \quad (5)$$

Here the Tafel slope on a natural logarithm basis reads $b_i = RT/\alpha_i F$, with α_i the charge transfer coefficient. The cathodic activation overpotential η_c is concentration independent. The anode adds, besides a concentration-independent part η_a, a concentration overpotential η_{lim}. This part is due to the dependence of the anodic half-reaction, Eq. (2), on the hydroxide concentration. For symmetric charge transfer, the anodic concentration-dependent Butler–Volmer equation $j = j_{*a}\left(\frac{c_a}{c}e^{\frac{\eta_a+\eta_{\text{lim}}}{b_a}} - e^{-\frac{\eta_a+\eta_{\text{lim}}}{b_a}}\right)$ gives for the total anodic activation losses

$$\eta_a + \eta_{\text{lim}} \approx b_a \operatorname{asinh}\left(\frac{j}{2j_{*a}}\frac{c_a}{c}\right). \quad (6)$$

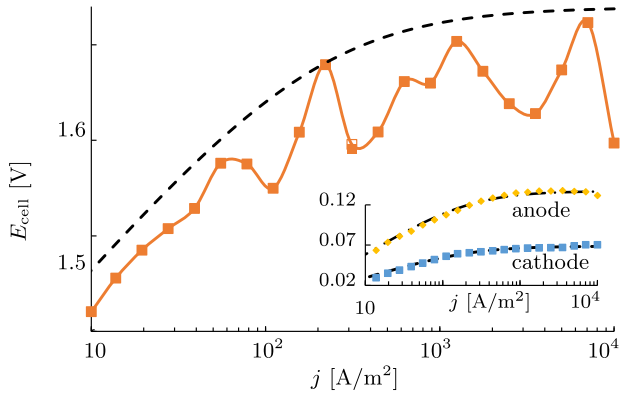

Fig. 3. The cell voltage, measured within a fraction of a second after the current has been switched off. An average over all conductivities is provided, excluding data points deviating more than 0.5 V from the dashed line, representing Eq. (7). The inset plot gives the IR-corrected overpotentials measured relative to the copper wire visible in Fig. 2, after subtracting the activation overpotentials. The dashed lines in the inset graph indicate $\ln \frac{j}{1+j/j_{\text{eq}}}$ times RT/F (60 mV/dec) and $RT/2F$ (30 mV/dec) for anode and cathode, respectively.

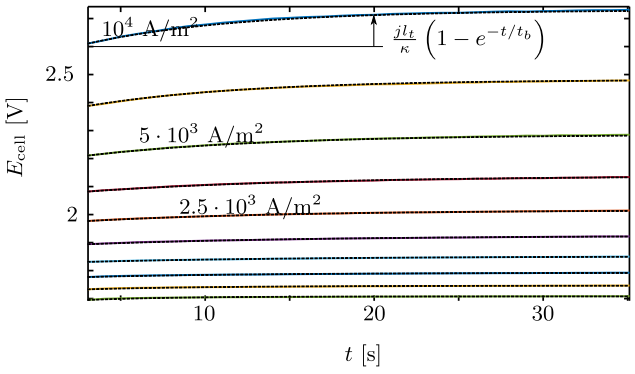

Fig. 4. The measured cell voltage increase for $c = 6$ M (solid lines) can be fitted well with Eq. (8) (dashed lines — approximately overlapping). The fitting parameters $l_t \approx 1.1$ mm and $t_b \approx 10$ s for the highest current density both only very slightly increase with decreasing current density, see Appendix A.

In writing Eq. (6) we assumed that the average hydroxide concentration at the anode surface, c_a, tends to the average bulk electrolyte concentration c for low overpotentials $\eta_a \lesssim b_a$.

Based on our experimental results, we introduce the following parametrization for the equilibrium voltage

$$E_{\text{eq}} = E_0 + \frac{7RT}{4F}\ln\left(\frac{j}{1+j/j_{\text{eq}}}\right), \tag{7}$$

see Section 4.1 for its justification. In the next section we will compare all semi-empirical expressions introduced here, with experimental results.

4. Experiments

4.1. Equilibrium voltage

The functional form of Eq. (7) is inspired by the Nernst equation for the reactions (1) and (2) assuming ideal unity activity coefficients [56,64]. The prefactor 7/4 derives from the sum of the stoichiometries 1/2 and 1/4 of hydrogen and oxygen, respectively, plus an additional $\sim RT/F$ that is introduced to provide a better fit with the current-interrupt data of Fig. 3. This Tafel slope was also found at low current densities $j < j_{*a}$ at the anode, as shown in the inset of Fig. 3. A possible cause may be an anodic side-reaction in which Ruthenium oxide corrodes to give dissolved RuO_4^{2-} [65], see also Appendix A and Section 5 for more information and discussion, respectively.

Eq. (7) can be derived assuming that the concentration of dissolved products involved in the Nernst equation is proportional to the current density. With a constant mass transfer coefficient, dissolved oxygen and hydrogen concentrations that are much higher than the solubility become proportional to the current density [66]. This can also be seen from the measurements in Refs. [39,40] where the cathode potential was found to increase with $\frac{RT}{2F}\frac{1}{\ln 10} \approx 30$ mV upon every decade of increase in current. For $j \gtrsim 10^3$ A/m^2 the potential flattened, similar to what can be seen in Fig. 3. We take this into account through the denominator $1 + j/j_{\text{eq}}$ in Eq. (7).

4.2. Ohmic losses

4.2.1. Electrolyte ohmic losses

The best fit of the ohmic term jl/κ in Eq. (4) to the experimental data was obtained with $l = 4.6$ mm. This is a surprisingly large value given that the separator has a thickness of only $l_s = 0.5$ mm. The separator porosity $\epsilon \approx 0.5 \pm 0.1$ and tortuosity $\tau \approx 1.55 - 2.84$ [18] combine to give a much lower effective thickness $l_s\tau/\epsilon \approx 1.5 - 3$ mm. Part of the ohmic drop, jl_t/κ with $l_t \approx 1$ mm, was found to arise transiently and will be discussed in the next section. The remaining $l - l_t = 3.6$ mm corresponds to a tortuosity $\tau \approx 3.6$, or MacMullin number $\tau/\epsilon = 7.2$, still above all experimental determinations of the separator tortuosity.

This situation is typical for zero-gap configurations, as argued in Ref. [5]. A conductivity of $\kappa = 138$ S/m at 80 °C and 30 w% electrolyte concentration would give an areal resistance of $(l - l_t)/\kappa = 0.26$ Ωcm^2 or $l/\kappa = 0.33$ Ωcm^2, both within the range of values listed there. In Ref. [5] simulations are discussed in which the electrode area that faces the separator was effectively made inactive by using a very high gas fraction inside the gap. For gas fractions in the bulk ranging from 0 to 0.6, areal resistances ranging from 0.194 to 0.361 Ωcm^2 were obtained. The measured ohmic drop can thus potentially be explained by a largely inactive electrode frontal area. To support this hypothesis, we found that the ohmic losses were not significantly impacted when a thin layer of epoxy glue (two-component epoxy resin and hardener, Bison Kombi) was applied to the front of both anode and cathode. Inactivity of the frontal electrode area without the epoxy layer present may arise, for example, due to blocking of the separator pores by a gas film, compression of the electrode, or reaction deposits [10]; a high local supersaturation of product gases in the poorly mixed region near the separator can further reduce the reactivity. However, the exact origin requires further investigation.

4.2.2. Bubble losses

Fig. 4 shows how, after the current is switched on, an additional voltage drop arise that is linear in the current density. This can be attributed to an ohmic drop in the electrolyte, since it was also observed between two copper wires placed on either side of the separator, see Fig. 2 and Appendix A. The associated e-folding time scale $t_b \sim 10$ s is smaller than the diffusive time-scale of the separator [55]. The diffusion potential would also lead to a decrease in the cell voltage [55]. We note that recently a similar potential increase was observed in proton exchange membrane electrolysers [67,68]. Very recently, the time-rate of change in the voltage of an alkaline electrolysis cell with a hydrophobic diffusion layer was used as a measure of bubble formation [69].

A time-scale of seconds correspond to that associated with the growth and detachment of bubbles at lower current densities and the formation of a haze of small bubbles at higher current densities, primarily at the cathode.

Inside the electrode openings, shielded from natural convection flows, bubbles can accumulate for several seconds before being swept away, as shown in Fig. 5 and the accompanying videos in the supplementary data of Appendix A. In Ref. [24], bubbles attached to the

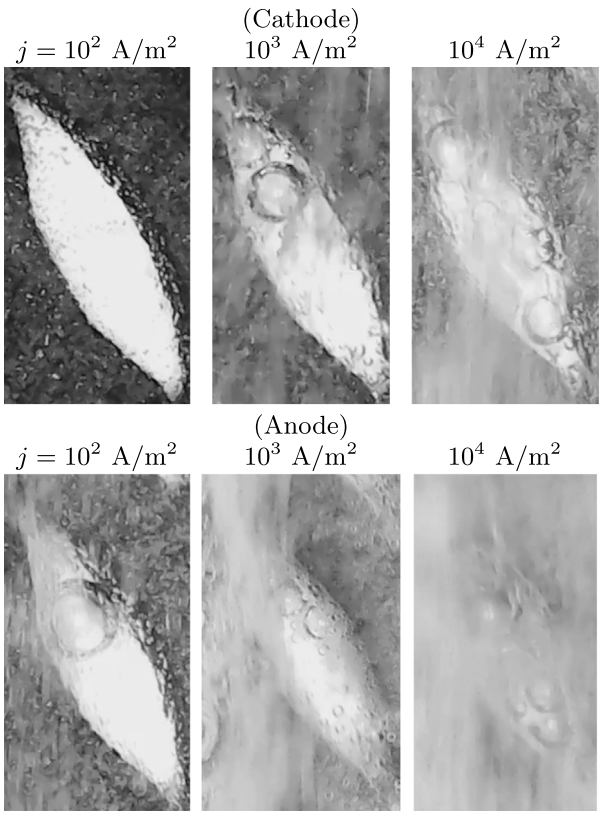

Fig. 5. Oxygen (top) and hydrogen (bottom) bubbles approximately $t = 3.7$ s after the current is switched on. After this time, primarily at the cathode, the visibility strongly deteriorates. An electrolyte concentration of $c = 6$ M and a container with a distance of 8 mm between the electrode and wall of the container was used for improved visibility. Small bubbles seem to be preferentially generated at the rims, while larger ones grow at the top of the electrode holes. Bubbles on the leeward bottom left rim are released while those at the top windward right rim tend to slide upwards. See Appendix A for videos of each image.

diaphragm were found mostly near the top of the electrode openings where they grew by diffusion. The final bubble size was found to primarily depend on the separator material.

Over the course of several seconds, the electrolyte became cloudy from a haze of small accumulating bubbles. From Fig. 5, this can be seen to happen primarily near the cathode. A simple differential equation for the gas fraction ε with a constant production term, and a removal term that is proportional to the gas fraction, reads along with its solution

$$\frac{d\varepsilon}{dt} = \frac{\varepsilon_\infty - \varepsilon}{t_b} \rightarrow \varepsilon = \varepsilon_\infty \left(1 - e^{-t/t_b}\right). \tag{8}$$

This solution is shown to accurately fit the data in Fig. 4. The time-scale $t_b \approx 10$ s only weakly decreases with increasing current density, see Fig. SI.2 in Appendix A. With a constant ε_∞, this admittedly simplified model can quantitatively describe the transient ohmic losses shown in Fig. 4. Using the Bruggemans correction factor [70,71] for spherical bubbles, the measured $l_t \approx l_{t0}/\epsilon_e \left(1-\varepsilon_\infty\right)^{1.5} \approx 1$ mm requires the ionic current to travel, for example, through a gas fraction of $\varepsilon_\infty = 0.55$ over a distance of $l_{t0} = 0.1$ mm or through $\varepsilon_\infty = 0.29$ over a distance of $l_{t0} = 0.2$ mm. These values correspond well to, and may therefore be explained by, the typical diameter and surface coverage of a layer of adhering bubbles [33]. Detached bubbles will further add to the ohmic drop.

Considering the electrode as a non-tortuous porous medium with porosity $\epsilon_e \approx 1/3$ and Tafel slope b, most of the current will be generated within a distance $\kappa\epsilon_e b/j$ [70]. Even for the highest conductivity used, this distance is already smaller than the electrode thickness for $j \gtrsim 2 \cdot 10^3$ A/m^2. Therefore, for the highest current densities, the rear of the electrode can be considered largely inactive. Since we already established that the front of the electrodes is also mostly inactive, we find that in a zero-gap configuration the side walls of the electrode openings will provide the majority of the reaction area. Fig. 5 and the videos in the supplementary data of Appendix A do indeed seem to show that most of the gas bubbles originate from these locations.

Table 1
Fitting parameters used in Eqs. (4)–(7), and (9). We assumed a constant temperature of $T = 300$ K throughout. The used electrodes have an open hole fraction of $\epsilon_e \approx 1/3$ and a thickness $l_e \approx 0.5$ mm. The indicated Tafel slopes b_i are on a natural logarithm base. .

E_0	1.38 V	l	4.6 mm
j_{eq}	200 A/m^2	l_t	1.1 mm
AR	17 μΩm^2	b_{lim}	1 V
j_{*c}	800 A/m^2	l_{lim}	0.8 mm
j_{*a}	200 A/m^2	κ_{lim}	1.63 S/m
b_c	52 mV/e	p	0.1
b_a	40 mV/e	q	1.77

In Refs. [54,55] we actually already noted, but could not explain, a transient increase in potential. We modeled the ohmic resistance by adding to the electrode thickness roughly the electrode size on both sides of the separator, using $\tau = 1.62$ giving $l = (1.5\text{ mm})\tau/\epsilon = 4.9$ mm, slightly more than the $l = 4.6$ mm we find here. In Ref. [70] we discuss also the data from a repeat experiment that is best fitted with $l = 4$ mm. These results shows that l is not exactly reproducible between experiments. It has been speculated that nano bubbles trapped inside the separator may play a role in increasing the resistance [5,25,26]. However, such bubbles would also decrease the effective diffusion coefficients inside the separator. To calculate the limiting current associated with global hydroxide depletion, we needed no such correction in Refs. [54,55] and used an effective separator thickness $(0.5\text{ mm})\tau/\epsilon = 1.62$ mm, using $\tau = 1.62$, with reasonable agreement. A much lower tortuosity could thus be used compared to that required to describe the ohmic drop. This may be explained by an additional electrolyte flux, in parallel to the one required for the current. Contrary to the current density [55], such an electrolyte flux can be assisted by advective mixing due to bubbles [72] and the natural convection flows they induce. As a result, inside the separator this additional flux may be more evenly distributed than the current density. This therefore provides some evidence that the additional resistance we find in a zero-gap configuration, both that almost immediately present and that arising transiently, arises external to the electrode.

4.2.3. Electrode ohmic losses

Subtracting from the measured cell voltage fits of all the other losses shows a remaining loss of about 0.17 V at 10^4 A/m^2 that is approximately linear in current density and independent of ionic conductivity, see Appendix A. Bubble-associated increased activation losses cannot explain these observations as they would require unrealistically high surface coverages [35].

Measuring the voltage drop over a narrow strip of electrode of known length and width, we measured a surprisingly high effective electrode resistivity of $\rho_e \approx 2 \cdot 10^{-6}$ Ωm. The electrode strip visible at the top of Fig. 2 has a width $w \approx 1.5$ cm and height $h \approx 4.5$ cm up to the position of the clamps. This gives a resistance $\rho_e h/l_e w \approx 12$ mΩ, or electrode-area-specific resistance $AR \approx 1.2 \cdot 10^{-5}$ Ωm^2, which is only slightly below the fitted value in Table 1. The small difference can be accounted for by additional electronic losses from the average distance that the current travels within the active part of the electrodes.

4.3. Activation overpotentials

4.3.1. Kinetic overpotentials

In Eqs. (4)–(6) we wrote the overpotential $\eta = \eta_c + \eta_a + \eta_{lim}$ as the sum of cathodic and anodic activation overpotentials, where we separate

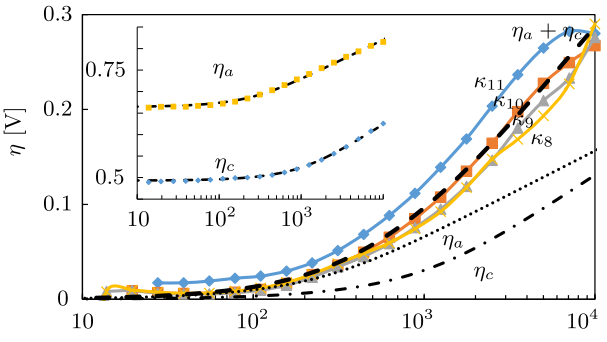

Fig. 6. The activation overpotential $\eta = E_{\text{cell}} - jl/\kappa - ARj$ for conductivities $\kappa > 20$ S/m for which the concentration overpotential η_{lim} is negligible. The inset plot shows the IR-corrected overpotentials η_a and η_c relative to the copper wire shown in Fig. 2, after subtracting $\ln \frac{j}{1+j/j_{\text{eq}}}$ times RT/F (60 mV/dec) and $RT/2F$ (30 mV/dec) for anode and cathode, respectively.

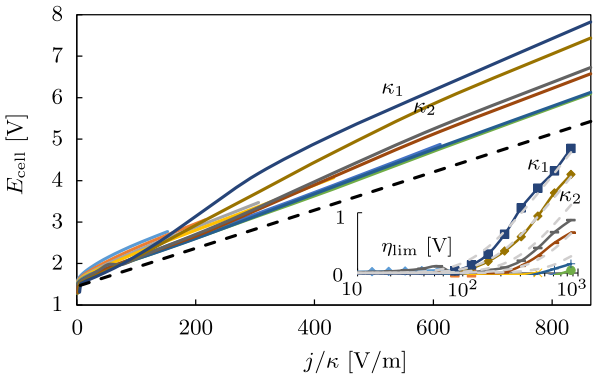

Fig. 7. The cell voltage recorded with the set-up of Fig. 2 for conductivities $\kappa_1 = 2.04$ S/m, $\kappa_2 = \sqrt{2}\kappa_1 = 2.89$ S/m, etcetera. The dashed line gives $E_0 + jl/\kappa$ using the parameters of Table 1. The inset plot gives the hydroxide depletion concentration overpotential $\eta_{\text{lim}} = E_{\text{cell}} - E_{\text{eq}} - \eta_a - \eta_c - jl/\kappa - ARj$, where the gray dashed lines give the parametrization of Eqs. (6)–(9).

the latter into a concentration-independent activation overpotential η_a and a concentration overpotential η_{lim} due to local anodic hydroxide depletion.

The total activation overpotential $\eta = E_{\text{cell}} - \left(E_{\text{eq}} + jl/\kappa + ARj\right)$, obtained using Eq. (7) and the fitting parameters in Table 1, is shown in Fig. 6. Only the highest four conductivities are displayed, for which η_{lim} is negligible.

Relative to a copper wire we measured η_c and η_a shown in the inset plot of Fig. 2. A cathodic Tafel slope $b_c = RT/\alpha_c F \approx 52$ mV/e was found or, multiplying with $\ln 10 \approx 2.3$, 120 mV/dec. This corresponds to a charge transfer coefficient of $\alpha = 1/2$, suggesting a Volmer rate-determining step. The cathodic effective exchange current density $j_{*c} \approx 800$ A/m^2 is high, owing to the excellent catalytic properties for the hydrogen evolution reaction of the used electrodes. The obtained anodic Tafel slope $RT/\alpha_a F = 40$ mV/e, or 92 mV/dec, corresponds to an anodic charge transfer coefficient of $\alpha_a \approx 0.65$. The anodic exchange current density $j_{*a} \approx 200$ A/m^2 was found to be lower than the cathodic one. Note that the validity of using a copper pseudo-reference electrode has not been established previously for the used conditions. The activation overpotentials shown in the main Fig. 6 were obtained from the cell voltage and therefore do not depend on, but show good agreement with, the measurements using this reference. While this is encouraging, this is no thorough proof that copper can always be accurately and stably be used as a reference in alkaline water electrolysis.

4.3.2. Resistive effects

Often much lower Tafel slopes are measured on Ruthenium oxides [73], although typically at very low current densities. Could the relatively high values we find perhaps be a result of transport limitations? A doubling in current density leads to a halving of the current penetration thickness and reactive surface area, leading to a doubling of the effective Tafel slope [70,74,75]. Two-dimensional simulations show something similar to this one-dimensional theoretical expectation [76]. This would imply that we observe twice the intrinsic kinetic Tafel slopes. However, in this case the effective exchange current density is predicted to be proportional to $\sqrt{\kappa}$ [70,75], something that is not observed in Fig. 6. It is presently unclear why no Tafel slope doubling can be observed.

The front of the electrode is likely always within the current penetration thickness $\kappa b_i/j$, but was shown to not significantly contribute to the reactivity. Alternatively, the two-dimensional nature of the electrodes and the spatial gas distribution invalidates the one-dimensional prediction of Tafel slope doubling. This warrants further investigation.

4.3.3. Concentration overpotential

Fig. 7 shows the recorded steady-state cell voltages as a function of the ratio j/κ. Most of the data collapses to a similar linear trend corresponding to ohmic losses. Some of the spread arises because the activation overpotentials depend on current density j rather than j/κ. The lowest conductivities $\kappa \leq \kappa_6$ or $c < 0.5$ M show pronounced additional losses η_{lim} that are shown in the inset plot and can be attributed to local hydroxide depletion. This data can be fit reasonably well using Eq. (6) with

$$\frac{c_a}{c} = \left(1 + \left(j/j_{\text{lim}}\right)^{pb_{\text{lim}}/b_a}\right)^{-1/p},$$
$$j_{\text{lim}} = \frac{2FD_- c}{l_{\text{lim}}}\left(1 + \left(\kappa/\kappa_{\text{lim}}\right)^q\right). \tag{9}$$

Here p, q, l_{lim}, and κ_{lim} area given in Table 1 and $D_- \approx 5.3 \cdot 10^{-9}$ m^2/s is the hydroxide ion diffusivity [77]. The factor two in Eq. (9) derives from a contribution of migration to the current density that, in steady state, is equal to that of diffusion [54,55]. The current density j_{lim} here is a characteristic value for which the hydroxide concentration at the anode surface starts to deplete *locally*. It differs from the limiting current density in Refs. [54,55] where the hydroxide concentration depleted in the entire anolyte. Overlimiting currents [78] beyond j_{lim} are possible and for $j \gg j_{*a}, j_{\text{lim}}$ Eqs. (5), (6), and (9) give $\eta_{\text{lim}} = b_{\text{lim}} \ln \frac{j}{j_{\text{lim}}}$. This logarithmic increase is clearly visible in the inset plot of Fig. 7. The effective length-scale $l_{\text{lim}} \approx 0.8$ mm in Eq. (9) corresponds to a distance $l_{\text{lim}}\epsilon_e \approx 0.3$ mm, of the order of the electrode thickness. As is further illustrated in Appendix A, the concentration polarization η_{lim} develops transiently over a diffusive time-scale of the order of a minute.

4.4. Almost-zero gap

Using the parameters of Table 1 in Eqs. (4)–(7) along with Eq. (9), a maximum relative difference with the experimental data below 6% was obtained, and below 2% for the highest four conductivities. We show an example of such a fit for $c = 6$ M in Fig. 8 in which also the various terms in Eq. (4) are indicated.

We see that at the highest current density, more than half of the overpotential comes from the separator ohmic losses jl/κ. To further investigate the partly responsible inactivity of the electrode area facing the separator, we introduced a small gap of 0.2 mm between the electrodes and the separator. Such almost-zero gap configurations have also been referred to as near zero-gap [79,80] or nearly zero gap [12].

We used nylon spacers, visible in Fig. 2, from which a hole with the size of the electrodes was cut out. Fig. 8 shows the resulting polarization curve, using a $c = 6$ M electrolyte, along with that of the original

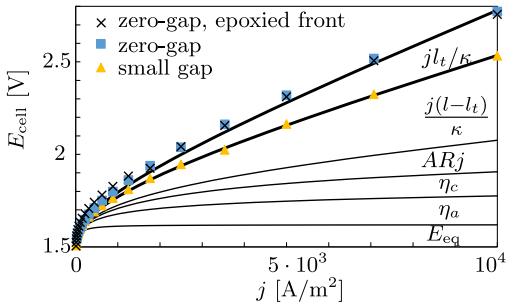

Fig. 8. The cell voltage recorded with the set-up of Fig. 2 showing that a gap of 0.2 mm between the electrodes and the separator (yellow triangles) significantly reduces the ohmic losses compared to the configuration without such a small gap (blue squares and black crosses). Covering with epoxy the area of the electrode that faces the separator seems to slightly increase the activation losses at low current densities, but does not significantly alter the ohmic losses. The solid lines give the various losses described by Eqs. (4)–(7) and Eq. (9) using the parameters of Table 1.

zero-gap configuration. The shown fits use the same parameters except that $l = 4.6$ mm for the zero-gap configuration is replaced by 3 mm for the almost-zero-gap configuration. This strong reduction in ohmic drop can be partially explained by the almost absent transient losses, see Appendix A. The applicable 3 mm is however even below $l - l_t = 3.6$ mm, despite the additional 2×0.2 mm $= 0.4$ mm gap. This can be explained by the more homogeneous current distribution that results when the electrode front becomes active.

Using $\kappa = 138$ S/m for 80 °C and 30 w%, the area-specific resistance (3 mm)$/\kappa = 0.22$ Ωcm^2 is lower than all of the 'zero-gap' results listed in Ref. [5], while simulations with a 0.2 mm gap and a high gas fraction of 0.6 showed a similar resistance of 0.19 Ωcm^2.

We note that a positive effect of a small gap has been suggested in the conclusions of Ref. [6] but was not quantified. Ref. [13] introduced a smaller gap < 0.15 mm, resulting in a much smaller decrease in losses then found here.

Upon introducing the small gap we also found a small, perhaps not significant, decrease of ∼ 10 mV in the equilibrium potential at low current densities. This can be explained by enhanced advection that transports out dissolved products.

5. Conclusions and discussion

We provided detailed measurements of the cell voltage of a lab-scale zero-gap alkaline water electrolysis cell over a wide range of current densities 10 A/m^2 $\leq j \leq$ 10^4 A/m^2 and electrolyte concentrations 0.08 M $\leq c \leq$ 6 M.

Using additional input from reference electrode and current-interrupt data, the cell voltage was split into equilibrium, activation, and ohmic components according to Eq. (4). The activation overpotentials could be described well with the Butler–Volmer equation provided that, for concentrations $c \lesssim 0.5$ M, the concentration polarization due to local anodic hydroxide depletion was taken into account. We provided a purely empirical equation (9) to describe these losses, which likely strongly depends on the specific electrode and separator properties, as well as local flow conditions.

The equilibrium potential E_{eq} was found to increase with increasing current density to above 1.6 V, as shown in Fig. 3. Apart from a high onset potential we found a high slope $\partial E_{eq}/\partial \ln j \approx 7RT/4F \approx 0.1$ V/dec below $j_{eq} \approx 200$ A/m^2, of which only $3RT/4F$ can be explained by dissolved oxygen and hydrogen. At current densities well below the anodic exchange current density $j_{*a} \approx 200$ A/m^2 an anodic Tafel slope RT/F was found that may be related to a parasitic side-reaction of the Ruthenium-based electrode. Since $j_{eq} \approx j_{*a}$, we cannot fully exclude the possibility that these losses are kinetic in nature. In this case, about RT/F of the $7RT/4F$ found with current-interrupt measurements, has to be attributed to measurement inaccuracy.

The non-uniqueness of the obtained fitting parameters illustrates the difficulty of untangling the various losses. Therefore, it is not surprising that there is an almost complete lack in literature of measurements of bubble-induced losses in a zero-gap configuration. We did not find any evidence of increased activation losses due to bubbles covering the surface, an effect that presumably is relatively small for the current densities $\leq 10^4$ A/m^2 studied.

The ohmic resistance was found to be much larger than that of the separator, consistent with the area between the electrode and the separator being inactive. This was confirmed by an experiment in which this part was covered with epoxy, giving a virtually indistinguishable polarization curve. This inactivity may be explained by blockage of the separator pores by gas, mechanical forces, and or deposits, requiring further investigation.

We also found a sizeable transient increase in the ohmic losses that can plausibly be attributed to gas bubbles, likely mostly inside the electrode holes, although we cannot with certainty exclude the possibility that also some gas may enter the separator. The less than perfect reproducibility of these losses can be attributed to the stochastic nature of bubbles and local flow conditions.

A small 0.2 mm gap sufficed to remove a large part of the bubbles losses, greatly improving upon the performance over a zero-gap configuration. Further studies may show alternative means to avoid bubble losses, like electrolyte flow, increased pressure, modified material wetting properties, and tailored electrode shapes. There are, however, several additional advantages to the simple solution of a small gap, including decreased separator damage, and likely strongly reduced gas cross-over. We observed a small decrease in equilibrium potential in the presence of a gap, which can be attributed to improved electrolyte advection decreasing the dissolved gas concentrations. A lower dissolved gas concentration at the separator surface will strongly decrease gas cross-over through the separator, increasing the operational window of electrolyzers.

CRediT authorship contribution statement

J.W. Haverkort: Conceptualization, Methodology, Validation, Formal analysis, Investigation, Writing - original draft, Visualization, Supervision, Project administration, Funding acquisition. **H. Rajaei:** Software, Validation, Formal analysis, Investigation, Writing - review & editing. Visualization.

Declaration of competing interest

The authors declare that they have no known competing financial interests or personal relationships that could have appeared to influence the work reported in this paper.

Appendix A. Supplementary data

Supplementary material related to this article can be found online at https://doi.org/10.1016/j.jpowsour.2021.229864. The following is the supplementary data related to this article:

- Additional data and graphs
- All videos:
  - Anode, 10^2 A/m^2
  - Anode, 10^3 A/m^2
  - Anode, 10^4 A/m^2
  - Cathode, 10^2 A/m^2
  - Cathode, 10^3 A/m^4
  - Cathode, 10^4 A/m^2

References

[1] R.L. Costa, P.G. Grimes, Electrolysis as a Source of Hydrogen and Oxygen, Tech. Rep, Allis-Chalmers Mfg. Co., Milwaukee, 1967.

[2] A.T. Kuhn, Industrial Electrochemical Processes, Elsevier Publishing Company, 1971.

[3] J. Divisek, Water electrolysis in a low and medium temperature regime, in: Electrochemical Hydrogen Technologies-Electrochemical Production and Combustion of Hydrogen, Elsevier, Oxford, 1990.

[4] R. Phillips, A. Edwards, B. Rome, D.R. Jones, C.W. Dunnill, Minimising the ohmic resistance of an alkaline electrolysis cell through effective cell design, Int. J. Hydrogen Energy 42 (2017) 23986.

[5] M.T. de Groot, A.W. Vreman, Ohmic resistance in zero gap alkaline electrolysis with a Zirfon diaphragm, Electrochim. Acta (2020) 137684.

[6] V. Kienzlen, D. Haaf, W. Schnurnberger, Location of hydrogen gas evolution on perforated plate electrodes in zero gap cells, Int. J. Hydrogen Energy 19 (1994) 729.

[7] H. Wendt, Neue konstruktive und prozeßtechnische Konzepte für die Wasserstoff-Gewinnung durch Elektrolyse, Chem. Ing. Tech. 56 (1984) 265.

[8] H. Vogt, G. Kreysa, Electrochemical reactors, in: Ullmann's Encyclopedia of Industrial Chemistry, 2000.

[9] P. Gallone, L. Giuffré, G. Modica, Developments in separator technology for electrochemical reactors, Electrochim. Acta 28 (1983) 1299.

[10] J. Divisek, P. Malinowski, Electrolyzer with sandwich arrangement of diaphragm and electrodes and method of producing the sandwich arrangement, 1988, US Patent 4, 773, 982.

[11] J. Fischer, H. Hofmann, G. Luft, H. Wendt, Fundamental investigations and electrochemical engineering aspects concerning an advanced concept for alkaline water electrolysis, AIChE J. 26 (1980) 794.

[12] J. Brauns, J. Schönebeck, M.R. Kraglund, D. Aili, J. Hnát, J. Žitka, W. Mues, J.O. Jensen, K. Bouzek, T. Turek, Evaluation of diaphragms and membranes as separators for alkaline water electrolysis, J. Electrochem. Soc..

[13] J. Divisek, P. Malinowski, Diaphragm for alkaline electrolysis and process for manufacture of diaphragm, 1987, US Patent 4, 636, 291.

[14] M.J. Lavorante, C.Y. Reynoso, J.I. Franco, Water electrolysis with Zirfon® as separator and NaOH as electrolyte, Desalin. Water Treat. 56 (2015) 3647.

[15] A. Manabe, H. Domon, J. Kosaka, T. Hashimoto, T. Okajima, T. Ohsaka, Study on separator for alkaline water electrolysis, J. Electrochem. Soc. 163 (2016) F3139.

[16] A. Manabe, M. Kashiwase, T. Hashimoto, T. Hayashida, A. Kato, K. Hirao, I. Shimomura, I. Nagashima, Basic study of alkaline water electrolysis, Electrochim. Acta 100 (2013) 249.

[17] P. Vermeiren, W. Adriansens, J.P. Moreels, R. Leysen, Evaluation of the Zirfon® separator for use in alkaline water electrolysis and Ni-H2 batteries, Int. J. Hydrogen Energy 23 (1998) 321.

[18] J. Rodríguez, S. Palmas, M. Sánchez-Molina, E. Amores, L. Mais, R. Campana, Simple and precise approach for determination of ohmic contribution of diaphragms in alkaline water electrolysis, Membranes 9 (2019) 129.

[19] M. Schalenbach, W. Lueke, D. Stolten, Hydrogen diffusivity and electrolyte permeability of the Zirfon PERL separator for alkaline water electrolysis, J. Electrochem. Soc. 163 (2016) 80.

[20] J. Brauns, T. Turek, Alkaline water electrolysis powered by renewable energy: A review, Processes 8 (2020) 248.

[21] P. Trinke, P. Haug, J. Brauns, B. Bensmann, R. Hanke-Rauschenbach, T. Turek, Hydrogen crossover in pem and alkaline water electrolysis: mechanisms, direct comparison and mitigation strategies, J. Electrochem. Soc. 165 (2018) F502.

[22] S. Sevda, X. Dominguez-Benetton, K. Vanbroekhoven, T.R. Sreekrishnan, D. Pant, Characterization and comparison of the performance of two different separator types in air–cathode microbial fuel cell treating synthetic wastewater, Chem. Eng. J. 228 (2013) 1.

[23] H. In Lee, D.T. Dung, J. Kim, J.H. Pak, S. k. Kim, H.S. Cho, W.C. Cho, C.H. Kim, The synthesis of a Zirfon-type porous separator with reduced gas crossover for alkaline electrolyzer, Int. J. Energy Res. 44 (2020) 1875.

[24] A.S. Strub, G. Imarisio, Hydrogen As an Energy Vector: Proceedings of the International Seminar, Held in Brussels, 12–14 February 1980 Springer Science & Business Media, 2013.

[25] S. Marini, P. Salvi, P. Nelli, R. Pesenti, M. Villa, M. Berrettoni, G. Zangari, Y. Kiros, Advanced alkaline water electrolysis, Electrochim. Acta 82 (2012) 384.

[26] M.R. Kraglund, Alkaline Membrane Water Electrolysis with Non-Noble Catalysts (Ph.D. thesis), Technical University of Denmark, 2017.

[27] R. Martinez Picazo, Optimal Electrode Material Study for an Alkaline Electrolyser Integrated Into a Micro-Scale Methanol Plant (Master's thesis), 2020.

[28] K. Zeng, D. Zhang, Recent progress in alkaline water electrolysis for hydrogen production and applications, Prog. Energy Combust. Sci. 36 (2010) 307.

[29] C.A.C. Sequeira, D.M.F. Santos, B. Šljukić, L. Amaral, Physics of electrolytic gas evolution, Braz. J. Phys. 43 (2013) 199.

[30] X. Zhao, H. Ren, L. Luo, Gas bubbles in electrochemical gas evolution reactions, Langmuir 35 (2019) 5392.

[31] A. Angulo, P. van der Linde, H. Gardeniers, M. Modestino, D.F. Rivas, Influence of bubbles on the energy conversion efficiency of electrochemical reactors, Joule 4 (2020) 555.

[32] J. Eigeldinger, H. Vogt, The bubble coverage of gas-evolving electrodes in a flowing electrolyte, Electrochim. Acta 45 (2000) 4449.

[33] R.J. Balzer, H. Vogt, Effect of electrolyte flow on the bubble coverage of vertical gas-evolving electrodes, J. Electrochem. Soc. 150 (2002) E11.

[34] N. Nagai, M. Takeuchi, T. Kimura, T. Oka, Existence of optimum space between electrodes on hydrogen production by water electrolysis, Int. J. Hydrogen Energy 28 (2003) 35.

[35] J. Dukovic, C.W. Tobias, The influence of attached bubbles on potential drop and current distribution at gas-evolving electrodes, J. Electrochem. Soc. 134 (1987) 331.

[36] C.W. Tobias, Effect of gas evolution on current distribution and ohmic resistance in electrolyzers, J. Electrochem. Soc. 106 (1959) 833.

[37] J. Rodríguez, E. Amores, CFD modeling and experimental validation of an alkaline water electrolysis cell for hydrogen production, Processes 8 (2020) 1634.

[38] J.A. Leistra, P.J. Sides, Hyperpolarization of gas evolving electrodes—I. Aqueous electrolysis, Electrochim. Acta 32 (1987) 1489.

[39] S. Shibata, Supersolubility of hydyogen in acidic solution in the vicinity of hydrogen-evolving platinum cathodes in different surface states, Denki Kagaku oyobi Kogyo Butsuri Kagaku 44 (1976) 709.

[40] S. Shibata, The concentration of molecular hydrogen on the platinum cathode, Bull. Chem. Soc. Japan 36 (1963) 53.

[41] H. Vogt, The rate of gas evolution of electrodes—I. An estimate of the efficiency of gas evolution from the supersaturation of electrolyte adjacent to a gas-evolving electrode, Electrochim. Acta 29 (1984) 167.

[42] L. Müller, M. Krenz, K. Rübner, On the relation between the transport of electrochemically evolved Cl2 and H2 into the electrolyte bulk by convective diffusion and by gas bubbles, Electrochim. Acta 34 (1989) 305.

[43] F. Yang, M.J. Kim, M. Brown, B.J. Wiley, Alkaline water electrolysis at 25 a cm- 2 with a microfibrous flow-through electrode, Adv. Energy Mater. (2020) 2001174.

[44] H. Rajaei, A. Rajora, J.W. Haverkort, Design of membraneless gas-evolving flow-through porous electrodes, J. Power Sources 491 (2021) 229364.

[45] I. Dedigama, P. Angeli, K. Ayers, J.B. Robinson, P.R. Shearing, D. Tsaoulidis, D.J.L. Brett, In situ diagnostic techniques for characterisation of polymer electrolyte membrane water electrolysers–flow visualisation and electrochemical impedance spectroscopy, Int. J. Hydrogen Energy 39 (2014) 4468.

[46] W. Xu, Z. Lu, X. Sun, L. Jiang, X. Duan, Superwetting electrodes for gas-involving electrocatalysis, Acc. Chem. Res. 51 (2018) 1590.

[47] S. Dutta, Technology assessment of advanced electrolytic hydrogen production, Int. J. Hydrogen Energy 15 (1990) 379.

[48] P. Tiwari, G. Tsekouras, K. Wagner, G.F. Swiegers, G.G. Wallace, A new class of bubble-free water electrolyzer that is intrinsically highly efficient, Int. J. Hydrogen Energy 44 (2019) 23568.

[49] M. Koj, J. Qian, T. Turek, Novel alkaline water electrolysis with nickel-iron gas diffusion electrode for oxygen evolution, Int. J. Hydrogen Energy 44 (2019) 29862.

[50] O. Winther-Jensen, K. Chatjaroenporn, B. Winther-Jensen, D.R. MacFarlane, Towards hydrogen production using a breathable electrode structure to directly separate gases in the water splitting reaction, Int. J. Hydrogen Energy 37 (2012) 8185.

[51] M.M. Bakker, D.A. Vermaas, Gas bubble removal in alkaline water electrolysis with utilization of pressure swings, Electrochim. Acta 319 (2019) 148.

[52] M.-Y. Lin, L.-W. Hourng, Ultrasonic wave field effects on hydrogen production by water electrolysis, J. Chin. Inst. Eng. 37 (2014) 1080.

[53] H. Matsushima, D. Kiuchi, Y. Fukunaka, Measurement of dissolved hydrogen supersaturation during water electrolysis in a magnetic field, Electrochim. Acta 54 (2009) 5858.

[54] J.W. Haverkort, H. Rajaei, Electro-osmotic flow and the limiting current in alkaline water electrolysis, J. Power Sources Adv. 6 (2020) 100034.

[55] J.W. Haverkort, Modeling and experiments of binary electrolytes in the presence of diffusion, migration, and electro-osmotic flow, Phys. Rev. A 14 (2020) 044047.

[56] D. Jang, H.-S. Cho, S. Kang, Numerical modeling and analysis of the effect of pressure on the performance of an alkaline water electrolysis system, Appl. Energy (2021) 116554.

[57] Ø. Ulleberg, Modeling of advanced alkaline electrolyzers: a system simulation approach, Int. J. Hydrogen Energy 28 (2003) 21.

[58] A. Roy, S. Watson, D. Infield, Comparison of electrical energy efficiency of atmospheric and high-pressure electrolysers, Int. J. Hydrogen Energy 31 (2006) 1964.

[59] P. Haug, M. Koj, T. Turek, Influence of process conditions on gas purity in alkaline water electrolysis, Int. J. Hydrogen Energy 42 (2017) 9406.

[60] T. Shimamune, E. Zimmerman, C. Andreasson, Electrode, 2009, US Patent 7, 566, 389.

[61] D. Pletcher, X. Li, S. Wang, A comparison of cathodes for zero gap alkaline water electrolysers for hydrogen production, Int. J. Hydrogen Energy 37 (2012) 7429.

[62] C. Henao, K. Agbossou, M. Hammoudi, Y. Dubé, A. Cardenas, Simulation tool based on a physics model and an electrical analogy for an alkaline electrolyser, J. Power Sources 250 (2014) 58.

[63] R.J. Gilliam, J.W. Graydon, D.W. Kirk, S.J. Thorpe, A review of specific conductivities of potassium hydroxide solutions for various concentrations and temperatures, Int. J. Hydrogen Energy 32 (2007) 359.

[64] C. Lamy, P. Millet, A critical review on the definitions used to calculate the energy efficiency coefficients of water electrolysis cells working under near ambient temperature conditions, J. Power Sources 447 (2020) 227350.
[65] S. Holmin, L.-Å. Näslund, Á.S. Ingason, J. Rosen, E. Zimmerman, Corrosion of ruthenium dioxide based cathodes in alkaline medium caused by reverse currents, Electrochim. Acta 146 (2014) 30.
[66] H. Vogt, The concentration overpotential of gas evolving electrodes as a multiple problem of mass transfer, J. Electrochem. Soc. 137 (1990) 1179.
[67] D. Guilbert, G. Vitale, Dynamic emulation of a pem electrolyzer by time constant based exponential model, Energies 12 (4) (2019) 750.
[68] A. Hernández-Gómez, V. Ramirez, D. Guilbert, B. Saldivar, Cell voltage static-dynamic modeling of a pem electrolyzer based on adaptive parameters: development and experimental validation, Renewable Energy 163 (2021) 1508.
[69] G. Tsekouras, R. Terrett, Z. Yu, Z. Cheng, G.F. Swiegers, T. Tsuzuki, R. Stranger, R.J. Pace, Insights into the phenomenon of 'bubble-free' electrocatalytic oxygen evolution from water, Sustain. Energy Fuels 5 (3) (2021) 808.
[70] J.W. Haverkort, A theoretical analysis of the optimal electrode thickness and porosity, Electrochim. Acta 295 (2019) 846.
[71] B. Tjaden, S.J. Cooper, D.J.L. Brett, D. Kramer, P.R. Shearing, On the origin and application of the bruggeman correlation for analysing transport phenomena in electrochemical systems, Curr. Opin. Chem. Eng. 12 (2016) 44.
[72] H. Vogt, K. Stephan, Local microprocesses at gas-evolving electrodes and their influence on mass transfer, Electrochim. Acta 155 (2015) 348.
[73] J. Yu, Q. He, G. Yang, W. Zhou, Z. Shao, M. Ni, Recent advances and prospective in ruthenium-based materials for electrochemical water splitting, ACS Catal. 9 (2019) 9973.
[74] J. Divisek, H. Schmitz, A bipolar cell for advanced alkaline water electrolysis, Int. J. Hydrogen Energy 7 (1982) 703.
[75] L.G. Austin, H. Lerner, The mode of operation of porous diffusion electrodes—I. Simple redox systems, Electrochim. Acta 9 (1964) 1469.
[76] Y. Nishiki, K. Aoki, K. Tokuda, H. Matsuda, Secondary current distribution in a two-dimensional model cell composed of an electrode with an open part, J. Appl. Electrochem. 16 (1986) 291.
[77] J. Newman, K.E. Thomas-Alyea, Electrochemical Systems, John Wiley & Sons, 2012.
[78] E.V. Dydek, B. Zaltzman, I. Rubinstein, D.S. Deng, A. Mani, M.Z. Bazant, Overlimiting current in a microchannel, Phys. Rev. Lett. 107 (2011) 118301.
[79] A. Vilanova, P. Dias, J. Azevedo, M. Wullenkord, C. Spenke, T. Lopes, A. Mendes, Solar water splitting under natural concentrated sunlight using a 200 cm2 photoelectrochemical-photovoltaic device, J. Power Sources 454 (2020) 227890.
[80] C.W. Raetzsch, H.J.F. Van, H. Cunningham, Diaphragm cell, 1975, US Patent 3, 910, 827.